Adaptively Encoding Multimode VCSEL With Spectral Efficient Data Formats for Seamless Wired-Wireless Network Coverage

Jui-Hung Weng, Wei-Chi Lo, Jiaxing Wang, Borching Su, Constance J. Chang-Hasnain, *Fellow, IEEE, Fellow, Optica*, and Gong-Ru Lin, *Fellow, IEEE, Fellow, Optica*

***Abstract*—The multiple data formats such as the quadrature amplitude modulation-orthogonal frequency division multiplexing (QAM-OFDM), generalized frequency division multiplexing (GFDM), and discrete multi-tone (DMT) are discussed for the 850-nm multi-mode vertical-cavity surface-emitting laser (MM-VCSEL) based transmission in back-to-back (BtB) and OM5-multimode fiber (OM5-MMF) cases. The 850-nm MM-VCSEL with 7-μm oxide aperture and 25-μm microstrip length was directly modulated using these advanced modulation schemes with high-spectral-usage bit-rate-coding efficiency. The MM-VCSEL biased at a DC of $20I_{th}$ exhibits about 6∼7 transverse modes. As bias current increases, the frequency response of the MM-VCSEL can be effectively broadened. Simultaneously, the relative intensity noise (RIN) around 10∼20 GHz also reduces to −146.6 dBc/Hz at 12 mA to further improve the transmitted signal-to-noise ratio (SNR) performance. However, the enhanced mode partition noise (MPN) occurs to degrade the SNR in frequency division multiplexing transmission in the low-frequency region. After using the pre-emphasis of data format, the QAM-OFDM transmission capacity can be improved to 136 Gbit/s in the BtB case and 100 Gbit/s in the 100-m OM5 MMF case. The promising GFDM for 5G/6G wireless with time/frequency synchronization insensitivity, low peak-to-average power ratio (PAPR), and low out-of-band radiation is also optimized for encoding the VCSEL under the trade-off between BER and PAPR. The PAPR of GFDM drops to 11 dB when setting the (K, M) = (128, 4) for achieving the complementary cumulative distribution function of PAPR as 0.1; however, which only enables BtB at 88 Gbit/s and 100-m-MMF at 68 Gbit/s as the SNR degrades in some blocked GFDM subchannels because of the over exhausted energy. To obtain the maximal bandwidth utilization efficiency, the DMT technique formed by adaptive QAM mapping and bit distribution is adopted to upgrade the data rate to 145 Gbit/s for the BtB link. Nevertheless, all coding formats enable the flexibility for seamless bridging of wired and wireless formats for future heterogeneous network transmission.**

***Index Terms*—Bit-loading intra-data-center, discrete multi-tone (DMT), generalized frequency division multiplexing (GFDM), M-ary quadrature amplitude modulation (M-ary-QAM), orthogonal frequency division multiplexing (OFDM), pre-distortion, seamless network, vertical cavity surface-emitting laser (VCSEL).**

I. Introduction

With the increased network users and devices, the popularity of networked devices is enhanced from 2.4 to 3.6 networked devices per capita from 2018 to 2023. The global mobile subscribers will exceed 70% of the global population by 2023 [1]. For the demand in social media, streaming services, and cloud computation, the data center is the only solution for sufficiently enhancing the transmission capacity. These increased data are circulated in the data center interconnect and then downloaded to the user. Service providers need to modify the existing architecture to cope with the growth of the data requirements. The drawback of electrical transmission lines such as high power consumption, strong signal attenuation, and signal distortion urges the fast-developing progress of optical communication technology, and the vertical-cavity surface-emitting laser (VCSEL) is the most universally applied laser for data-center communication with low power consumption, high conversion efficiency, inexpensive fabrication, high reliable manufacture [2], [3], modulated in high-speed with low bias current.

In addition to the development of the high-speed VCSEL, the data format is another method to effectively prompt the whole transmission capacity. With the development of high-speed transmission, the data rate provided by NRZ-OOK can no longer meet the high-speed demand. The signal format has evolved from the original non-return-to-zero on-off keying (NRZ-OOK) data to the later 4-level pulsed amplitude modulation (PAM-4) format for obtaining the double data rate. In addition to the PAM-4 format, the quadrature amplitude modulation-orthogonal frequency division multiplexing (QAM-OFDM) data can achieve a higher data rate by analog modulation in optical communication [4]. The use of more complex computing modulation for high-quality transmission has become a current trend because of the improvement of hardware computing capacity. To reduce the cost of data center operation, the analyzed software technologies such as mathematical tools and machine learning are implemented to prompt efficiency according to the traffic history [5],

Manuscript received 10 April 2024; revised 16 July 2024; accepted 2 August 2024. Date of publication 7 August 2024; date of current version 16 December 2024. This work was supported by National Science and Technology Council, Taiwan, under Grant NSTC 112-2119-M-002-013-, Grant 112-3111-E-992-001, Grant 112-2221-E-002-176-MY3, Grant 113-2119-M-002-023, and Grant 113-2221-E-002-101-MY3. *(Corresponding author: Gong-Ru Lin.)*

Jui-Hung Weng, Wei-Chi Lo, and Gong-Ru Lin are with the Graduate Institute of Photonics and Optoelectronics and the Department of Electrical Engineering, National Taiwan University, Taipei 10617, Taiwan (e-mail: grlin@ntu.edu.tw).

Jiaxing Wang and Constance J. Chang-Hasnain are with Berxel Photonics Inc., Shenzhen 518071, China.

Borching Su is with the Graduate Institute of Communication Engineering, National Taiwan University, Taipei 10617, Taiwan.

Color versions of one or more figures in this article are available at https://doi.org/10.1109/JLT.2024.3439875.

Digital Object Identifier 10.1109/JLT.2024.3439875

[6]. Using dynamic learning tools to predict modulation schemes can reduce network margins and provide optimized data rates. Network failures become predictable via the cognitive network. In addition, transferring traffic appropriately during the off-peak period avoids network congestion [7]. By flexible modulation, more reconfigurable and adjustable networks balance the distance and capacity of data transmission [8]. Software-aided technologies for network control and management are emerging in recent studies, indicating that flexible modulation schemes are mandatory to support multiple networking scenarios.

Except for the currently available orthogonal frequency division multiplexing (OFDM), the generalized frequency division multiplexing (GFDM) based on a multicarrier filter bank is also a promising format for wireless links, as it releases the need for time and frequency synchronization (insensitive to frequency offset and phase noise) [9], [10], [11], [12]. Its low peak-to-average ratio (PAPR) can be achieved by shaping the pulse in individual resource elements to improve the nonlinear distortion, increase the power amplifier efficiency, and promote data transmission performance. Besides, an appropriate prototype filter can be applied to reduce the out-of-band radiation (OOBR) [13], [14]. For improving the efficient usage of the allowable spectral bandwidth in the wireless application, such GFDM format accomplishes time-frequency flexible modulation with low-OOBR in cognitive networks, which concurrently allows unlicensed secondary users to exploit the spectral hole [15]. Moreover, the radio-over-fiber (RoF) technology based on optical self-heterodyne technology can overcome the bottlenecks of the current front-haul system to implement the high-speed seamless network at a relatively low cost because of the local-oscillator-free architecture at remote nodes [16], [17], [18]. To maximize spectral usage efficiency, the bit-loaded discrete multi-tone (DMT) format has also emerged in contrast to the traditional OFDM format with a fixed QAM mapping level for all subcarriers, which effectively skips the defective subcarrier induced by notched frequency response with enlarged BER and deteriorated constellation [19]. According to the spectral SNR response of a channel, each subcarrier is assigned individual bit-loading to properly configure the adaptive QAM mapping level [20], [21], [22]. Such a spectrally scaled bit distribution can manage the subcarrier with better SNR to carry more bits via a higher-ordered QAM mapping level for enhanced stability during transmission. As different photonic front-haul systems have successively been proposed to build up the seamless convergence of optical-wired and microwave-wireless networks, the optical front-haul transmitter with high spectral efficiency is demanded to perform the subcarrier-multiplexed and multi-band-utilized data transmissions for different wired and wireless bands configured for future networks.

In this work, the MM-VCSEL with an optimized design of its transmission microstrip length is employed to carry various data formats such as OFDM/GFDM/DMT for back-to-back (BtB) and 100-m OM5-MMF transmissions. For flexibly selecting the modulation strategy, the pre-distortion techniques are demonstrated to overcome insufficient or declined channel responses for optimizing the transmission capacity. In addition, the matrix-based GFDM is proposed and analyzed for real-valued output and low PAPR. The greedy-algorithm-based bit distribution in DMT format is demonstrated to achieve maximal spectrum efficiency. In addition, the first time experimentally confirms that the SNR degradation in the low-frequency region is caused by the mode partition noise (MPN) effect.

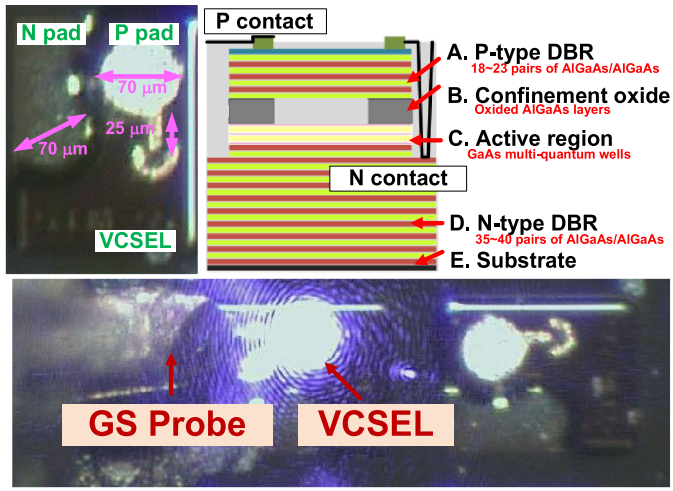

Fig. 1. Top: The microscopic graph and 3D schematic structure of the MM-VCSELs. Bottom: The photographs of the MM-VCSEL lighting up by the GS probe.

II. Experimental Setup

A. Material Structure and Device Configuration of the Oxide-Confined MM-VCSEL With Microstrip Transmission Contact

The upper part of Fig. 1 exhibits the microscopic photograph and 3D schematic diagram of the MM-VCSEL. In this work, the MM-VCSELs are grown on a 6-inch wafer. In the beginning, the n-GaAs buffer layer was deposited on a substrate to increase the success probability of the MM-VCSEL fabrication. Then, 35-40-pair $Al_{0.9}Ga_{0.1}As/Al_{0.12}Ga_{0.88}As$ layers were deposited as the n-type DBR structure on the n-type buffer layer. Next, the InGaAs MQW active layer was fabricated on the n-type DBR layer. The 98% AlGaAs oxidation layer was formed upon the MQW active layer to confine the mode of the MM-VCSEL. The aperture size of the MM-VCSEL in this work is designed as 7 μm.

Then, the 18-23 pair $Al_{0.9}Ga_{0.1}As/Al_{0.1}2Ga_{0.88}As$ DBR structures as the p-type layer were grown on the 98% AlGaAs oxidation layer. Finally, the p^{++}-type GaAs contact layer as the ohmic contact was deposited on the p-type DBR layer. For the metal contacts, the p-type metal contact was grown on the p^{++}-type ohmic contact. After the deep trench etching process, the n-type metal contact is fabricated on the n-type buffer layer. For suppressing the parasitic capacitance and chip size, the GS metallic coplanar electrode pads were utilized. To connect with an Au hemi-ring and the circular pad, the transmission microstrip was used and optimized at 25 μm to decrease the substrate parasitic capacitance. This phenomenon suppresses the low-pass filter effect to enhance the modulation bandwidth.

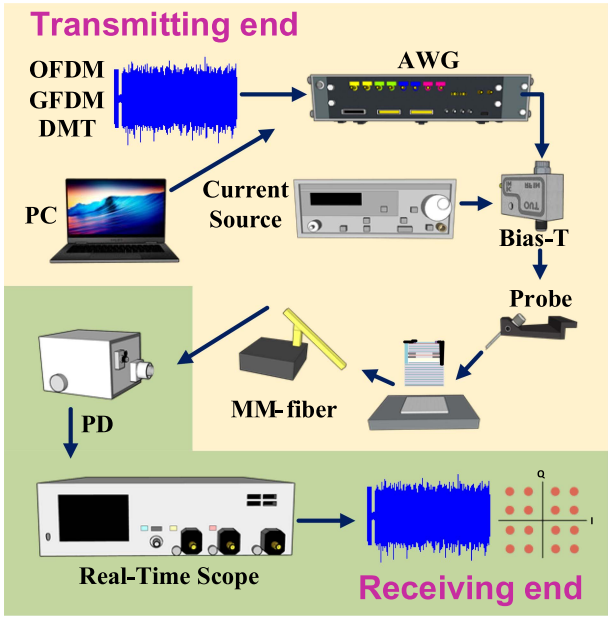

Fig. 2. The experimental setup for the 850-nm VCSEL carrying the OFDM/GFDM/DMT signals.

B. Back-to-Back and OM5-MMF Testing Link for the MM-VCSEL Data Transmission

The experimental setup of directly modulated 7-μm -aperture multi-mode VCSEL with 25-μm transmission microstrip is demonstrated in Fig. 2 to compare OFDM, GFDM, and DMT performances for 100-m OM5-MMF transmission. At the transmitting end, OFDM, GFDM, and DMT signals with 256 symbols were formed by a homemade MATLAB program and synthesized by a 45-GHz arbitrary waveform generator (AWG, Keysight M8194A) implementing the digital-to-analog conversion (DAC) with 8-bit resolution at a sampling rate of 120 GS/s. The DC bias current provided by a laser diode controller (ILX Lightwave, LDX-3210) and the AC signal synthesized by an AWG were coupled by a bias-tee (Anritsu, V250) with an analog bandwidth of 65-GHz. A 67-GHz broadband ground-signal (GS) microprobe (GGB 67A-GS-125-DP) with a pitch interval of 125 μm was used to directly modulate the VCSEL. The VCSEL was stability controlled at 20°C by a liquid-cooling heat sink (Deryun, DFC-4PT03) and vacuum on the probe station to maintain stability.

At the receiving end, after 100-m OM5 MMF transmission, a 22-GHz PIN photodetector (PD, New Focus 1484-A-50) with a maximal conversion gain of 65 V/W carried out the photoelectric conversion from the optical signal coupling to lensed MMF (SHUODA). The converted electric signal was received by the ATI channel with the analog-to-digital conversion (ADC) at a sampling rate of 200 GS/s with 8-bit resolution in a 70-GHz real-time digital phosphor oscilloscope (DPO, Tektronix DPO77002SX). A handmade MATLAB program demodulated the received OFDM, GFDM, and DMT data streams. Finally, the transmission parameters such as SNR, BER, and constellation plots were analyzed.

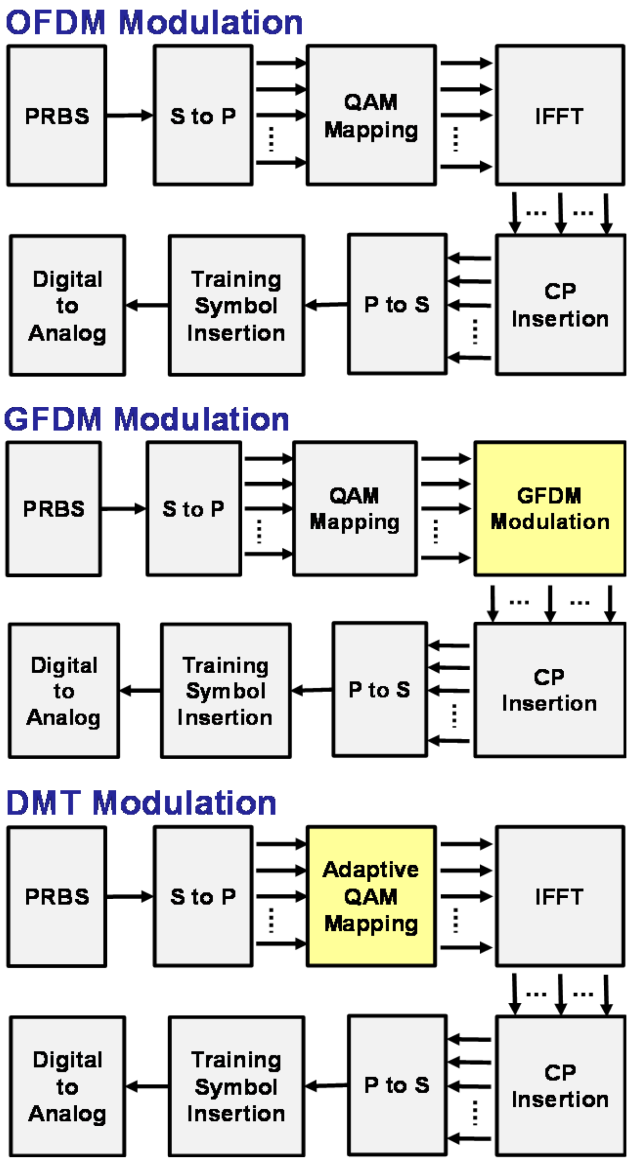

Fig. 3. The block diagrams of QAM-OFDM/GFDM/DMT algorithms.

C. Flow Charts for the OFDM, GFDM, and DMT Formats

The algorithms of QAM-OFDM, QAM-GFDM, and DMT data formats are illustrated in Fig. 3. For the QAM-OFDM, pseudorandom binary sequence (PRBS) data with a length of $2^{15} - 1$ was initially generated. After the serial to parallel conversion, the 16-QAM constellation mapping to complex value allocated to the OFDM subcarrier for inverse fast Fourier transform (IFFT). In the difference between GFDM and OFDM, the GFDM data format does not simply use the IFFT process but divides it into a matrix form represented by the K×M.

For the GFDM modulation, K is the subcarrier to perform the IFFT first, and M is the sub-symbol to execute the FFT first. The characteristic of the low PAPR in GFDM comes from multiple filtering. The rule of $N = K \times M$ must be met and $N = 512$ is presetting as the FFT size used in this algorithm. DMT is an extension of OFDM data formats to select adaptive QAM level mapping to allocate bits in each used subcarrier for

optimal spectral utilization efficiency. The Hermitian symmetry in the frequency domain must be achieved for the real-valued waveform in the time domain to satisfy the limitation of the photodetector with only receiving amplitude signals. To evaluate the cost in the optical layer, both OFDM and GFDM signals have specific requirements with a real-valued signal output that the photodetector can entirely receive. Therefore, this research includes the use of Hermitian symmetry to achieve real-valued signal output in GFDM modulation. The cyclic prefix (CP) can eliminate inter-symbol interference (ISI) and inter-carrier interference (ICI) after 100-m OM5-MMF transmission. The CP ratio was set as 1/32 of FFT size at this time. After applying the CP to three modulation schemes, the parallel to serial conversion was performed. Adding the training symbol in front of OFDM, GFDM, and DMT waveforms to capture the beginning of the signal during demodulation and estimate a channel response for equalization. Finally, AWG converted the OFDM, GFDM, and DMT signals from digital to analog.

D. Designing Principle and Algorithm of the GFDM Format

Fig. 13 shows the implementation of the time/frequency transformation matrix in GFDM data format. The resource elements are split into a two-dimensional time-frequency transformation matrix. For the transformation matrix, GFDM data format can flexibly select the single-carrier frequency-division equalization (SC-FDE) to transmit symbols in series with N sub-symbols, and the OFDM to send parallel N orthogonal subcarriers. The GFDM data format can be achieved by modifying the K and M sizes of the time-frequency transformation matrix. The SC-FDE and OFDM data formats are the two extreme modulation strategies of the GFDM. Following the rule of $N = K \times M$, the OFDM format is set as $N = K$, and the SC-FDE format is set as $N = M$. The SC-FDE data format directly transmits the data in the time domain.

Then, the data passes through the fast Fourier transform (FFT) to compensate in the frequency domain. The converted data is equalized and transformed to the original data by using the inverse FFT process. As compared to the OFDM data, the equalized method for SC-FDE data is more difficult. Each symbol of the SC-FDE data format utilizes the entire data bandwidth to provide the power-efficient modem. The OFDM data format delivers the data in the frequency domain. The data is converted by the IFFT process at the transmitted end and transformed back by the FFT technology at the received end. The equalizer is utilized to compensate for the OFDM data. However, the OFDM data usually exhibits high PAPR and large OOBR problems. First, the QAM mapping data is allocated into $N = K \times M$ data matrix form. Then, the IFFT is performed on each column on K subcarriers and the FFT is executed on each row on M sub-symbols. In addition, the appropriate prototype filter is selected as the characteristic matrix for improving GFDM performance. After applying the characteristic matrix in the GFDM process, the FFT is implemented on K subcarriers, and the matrix is reshaped into one row for the IFFT process at the end. However, to satisfy Hermitian symmetry before the last IFFT operation, the conjugate symmetric condition should be considered in the form of the data matrix. The mentioned matrix-based GFDM modulation process can be described by the following derivation,

$$\mathrm{X_f} = \mathrm{W_K}\left[\mathrm{W_K^H D W_M}\right]\overline{\mathrm{G}}, \tag{1}$$

where D is the data matrix; $\overline{\mathrm{G}}$ is the characteristic matrix of GFDM; $\mathrm{W_K^H W_K}^{\mathrm{H}}$ is the IFFT along the K direction; $\mathrm{W_K}$ is the FFT along the K direction, $\mathrm{W_M}$ is the FFT in the M direction. To simplify the GFDM process, the characteristic matrix is set to all one matrix this time. When $\overline{\mathrm{G}}$ is all one matrix, the $\mathrm{X_f}$ can be simplified as shown below,

$$\mathrm{X}_f = \mathrm{D W_M}, \tag{2}$$

The constraint needs to be followed to achieve the characteristic of conjugate symmetry in the K direction.

$$\mathrm{X}_f = \mathrm{J_K X}_f^*, \tag{3}$$

Then, the elements in the following (4) can be obtained by combining the prototype simplification and the conjugate symmetry in the K direction.

$$\begin{aligned} \mathrm{DW_M} &= \mathrm{X_f} = \mathrm{J_K X_f^*} = \mathrm{J_K D^* W_M^*} = \mathrm{J_K D^* W_M^{-1}} \\ \mathrm{DW_M^2} &= \mathrm{J_K D^*} \\ \mathrm{D} &= \mathrm{J_K D^* \overline{J}_M}, \end{aligned} \tag{4}$$

The $\mathrm{W_M}^2$ is a permutation matrix sign as $\overline{\mathrm{J}}_\mathrm{M}$. The $\overline{\mathrm{J}}_\mathrm{M}$ can be described as below,

$$\overline{\mathrm{J}}_\mathrm{M} = \begin{bmatrix} 1 & 0^{\mathrm{T}} \\ 0 & \mathrm{J_{M-1}} \end{bmatrix}, \tag{5}$$

Because of the symmetry in the K direction, the $\overline{\mathrm{J}}_\mathrm{M}$ matrix can be simplified into two small matrices, which is equivalent to swapping the top and bottom in half and then rearranging them to form the D matrix.

$$\mathrm{D} = \begin{bmatrix} \mathrm{D}_1 \\ \mathrm{D}_2 \end{bmatrix} = \mathrm{J_K} \begin{bmatrix} \mathrm{D}_1^* \\ \mathrm{D}_2^* \end{bmatrix} \overline{\mathrm{J}}_\mathrm{M} = \begin{bmatrix} \mathrm{J_{K/2} D}_2^* \\ \mathrm{J_{K/2} D}_1^* \end{bmatrix} \overline{\mathrm{J}}_\mathrm{M}, \tag{6}$$

From (6), the D_1 and D_2 can be represented as below,

$$\begin{aligned} \mathrm{D}_1 &= \mathrm{J_{K/2} D}_2^* \overline{\mathrm{J}}_\mathrm{M} \\ \mathrm{D}_2 &= \mathrm{J_{K/2} D}_1^* \overline{\mathrm{J}}_\mathrm{M}, \end{aligned} \tag{7}$$

According to the conjugate symmetry of $\mathrm{X_f} = \mathrm{J_K X_f}^*$, the $\mathrm{X_f}$ matrix is cut into upper and lower halves, as shown below,

$$\mathrm{X_f} = \begin{bmatrix} \mathrm{X}_1 \\ \mathrm{X}_2 \end{bmatrix} = \begin{bmatrix} \mathrm{J_{K/2} X}_2^* \\ \mathrm{J_{K/2} X}_1^* \end{bmatrix}. \tag{8}$$

Then, $\mathrm{X_f}$ can be reshaped into a vector as $\mathrm{x_f}$, as shown in (9).

$$\mathrm{x_f} = \mathrm{vec}\left(\mathrm{X_f^T}\right) = \mathrm{vec}\left(\begin{bmatrix} \mathrm{X}_1^{\mathrm{T}} & \mathrm{X}_2^{\mathrm{T}} \end{bmatrix}\right). \tag{9.1}$$

Nevertheless, the ultimate goal is to have conjugate symmetry by $\mathrm{x_f} = \mathrm{J_{KM} x_f}^*$. The output waveform can be real-valued after IFFT operation in the last layer of GFDM modulation. The $\mathrm{X_f}$ should be represented as

$$\mathrm{X_f} = \mathrm{J_K X_f^* J_M}. \tag{9.2}$$

Therefore, D must satisfy the diagonal conjugate symmetry. From the abovementioned discussion, (10) can be derived

from (4).

$$\mathrm{DW_M} = \mathrm{X_f} = \mathrm{J_K X_f^* J_M} = \mathrm{J_K D^* W_M^* J_M}$$
$$\mathrm{D} = \mathrm{J_K D^* W_M^{-1} J_M W_M^{-1}}. \tag{10}$$

where $\mathrm{W_M}^{-1}\mathrm{J_M W_M}^{-1}$ is a diagonal matrix and the absolute values in diagonal elements are all one value. The $\mathrm{Q_M}$ is proposed to replace $^{-1}$ as shown below,

$$\mathrm{Q_M} = \mathrm{W_M^{-1} J_M W_M^{-1}}$$
$$\mathrm{Q_M Q_M^*} = \mathrm{I_M}, \tag{11}$$

If M is even, the $\mathrm{Q_M}$ has the diagonal characteristic, as shown in (12).

$$\mathrm{Q_M} = \mathrm{diag}\left(\begin{bmatrix} \mathrm{q} \\ -\mathrm{q} \end{bmatrix}\right), \tag{12}$$

where the q is represented as shown below,

$$\mathrm{q} = \begin{bmatrix} 1 \\ \mathrm{e}^{-\mathrm{j}2\pi/\mathrm{M}} \\ \mathrm{M} \\ \mathrm{e}^{-\mathrm{j}2(\mathrm{M}-1)\pi/\mathrm{M}} \end{bmatrix}, \tag{13}$$

By replacing the $\mathrm{W_M}^{-1}\mathrm{J_M W_M}^{-1}$ with $\mathrm{Q_M}$, D can be modified as below,

$$\mathrm{D} = \mathrm{J_K D^* Q_M}, \tag{14}$$

Based on (6) and (14), $\mathrm{D_1}$ and $\mathrm{D_2}$ are real-valued signals and shown as below

$$\mathrm{D_1} = \mathrm{J_{K/2} D_2^* Q_M}$$
$$\mathrm{D_2} = \mathrm{J_{K/2} D_1^* Q_M}. \tag{15}$$

If the abovementioned rules in the data domain are followed, the real-valued waveform after the GFDM process can be obtained as well.

III. Result and Discussion

A. Lasing and Modulation Performances of the MM-VCSELs

The power-to-current (P-I) curve and slope efficiency of the MM-VCSEL with different bias currents are shown in Fig. 4(a), indicating that the MM-VCSEL exhibits its threshold current ($\mathrm{I_{th}}$) of 0.65 mA, the maximal output power of 3.74 mW, and slope efficiency in the linear region of 0.28 W/A. In typically microwave systems, the characteristic resistance of 50 Ω is used as a benchmark for minimal loss. The differential resistance obtained from the voltage-to-current (V-I) curve shown in Fig. 4(b) is 63.3 Ω at 12 mA. The signal reflection induced by the impedance mismatching will reduce the signal amplitude. The reflection coefficient (Γ) of the MM-VCSEL can be defined as $\Gamma = (\mathrm{Z_{VCSEL}}\text{-}\mathrm{Z_{RF}})/(\mathrm{Z_{VCSEL}}+\mathrm{Z_{RF}})$ where the $\mathrm{Z_{VCSEL}}$ is the impedance of the MM-VCSE, and the $\mathrm{Z_{RF}}$ is the characteristic impedance of 50 Ω in microwave circuits. By defining the voltage standing wave ratio (VSWR) as $\mathrm{VSWR} = (1+\Gamma)/(1\text{-}\Gamma)$ and the return loss ($\mathrm{R_L}$) as $\mathrm{R_L} = \text{-}20\log|\Gamma|$, the corresponding reflection coefficient of MM-VCSEL is 0.11 to obtain the VWSR of 1.24 and the return loss of 19.17 dB. Fig. 4(c) reveals the optical spectrum of MM-VCSEL at $20\mathrm{I_{th}}$. There are about 7 modes with a central wavelength of 856.3 nm, mode spacing of 0.52 nm, and a root-mean-square linewidth of 0.89 nm to affect modal dispersion after fiber transmission.

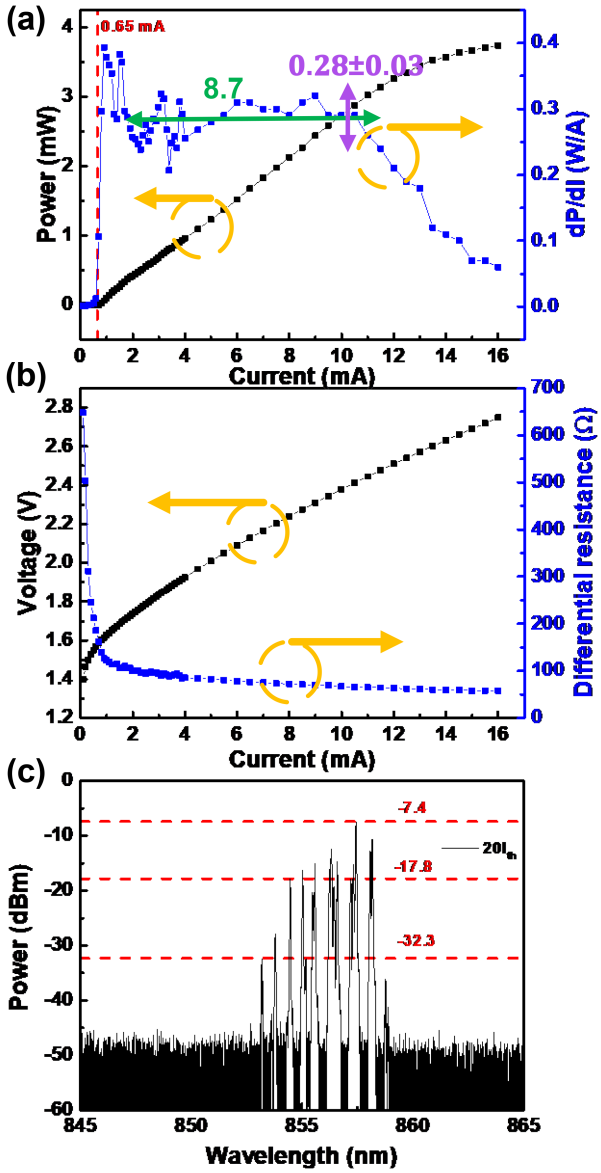

Fig. 4. The (a) P-I and δP/δI, (b) V-I and δV/δI curves, and the (c) optical spectrum of the MM-VCSEL.

It is necessary to analyze the small-signal modulation to discuss the performance of MM-VCSEL in high-speed transmission. The formula of resonance frequency and D factor can be described as [23]

$$\mathrm{D} = \sqrt{\frac{\mathrm{V_g} \times (\partial \mathrm{g}/\partial \mathrm{N}) \times \eta_\mathrm{i}}{4\pi^2 \times \mathrm{q} \times \mathrm{V_p}}}, \tag{16}$$

where D factor represents the modulation efficiency, ν_g is the group velocity of light, $\partial \mathrm{g}/\partial \mathrm{N}$ is the differential gain, q is the elementary charge, $\mathrm{V_p}$ is the effective mode volume, η_i the current injection efficiency as the fraction of the terminal current

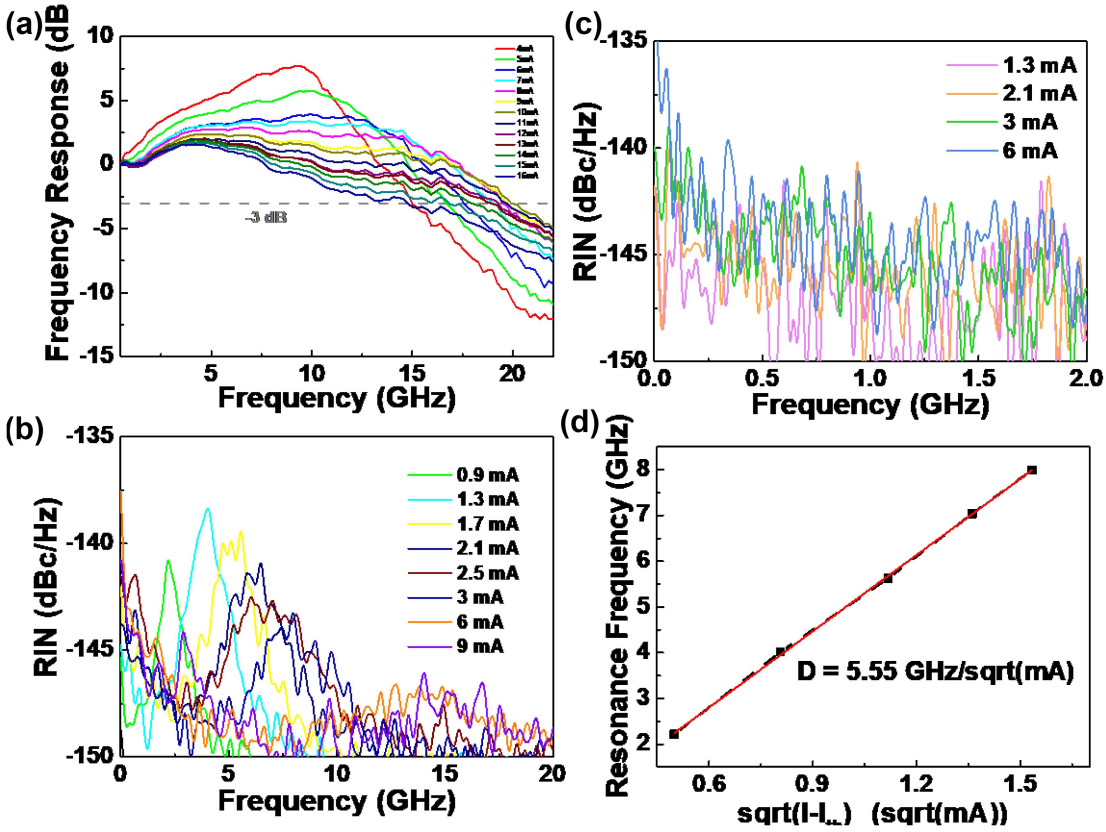

Fig. 5. The (a) frequency response, (b) RIN, (c) MPN spectrum, and (d) D factor of the MM-VCSEL.

that generates carrier in the active layer.

$$f_R = D \times \sqrt{I - I_{th}}, \tag{17}$$

where f_R indicates the relaxation oscillation frequency, which is proportional to the root of the bias current when the bias current is much greater than the threshold current. Fig. 5(a) shows the frequency response of the MM-VCSEL. As the bias current increases, the modulated throughput of the MM-VCSEL becomes flat and broad. The 3-dB bandwidth also increases from 14.5 GHz to 20.1 GHz when the DC enlarges from 4 mA to 10 mA. However, the 3-dB bandwidth decreases to 15 GHz because of the power saturation induced by the damping effect. The RIN spectrum of MM-VCSEL is illustrated in Fig. 5(b). When the bias rises from 0.9 to 9 mA, the resonance noise peak is gradually attenuated from −138.4 to −146.9 dBc/Hz, and the relaxation oscillation frequency upshifts from 4 to 15.1 GHz to be buried in the shot noise. Because the relaxation oscillation frequency is proportional to 3 dB bandwidth, the MM-VCSEL usually operates at a high bias current to avoid the relaxation oscillation frequency from affecting high-speed transmission. The stimulated recombination exhausts the local carriers at the high mode intensity region called the spatial hole burning effect (SHB) [24], [25], [26], [27], [28]. The MPN originated from the overlapped competition within the different transverse modes in the insufficient carrier density region will degrade the transmission performance in the low-frequency region. The RIN in the low-frequency region is especially observed to analyze the MPN, which dominates the noise in the low-frequency region from 10 to 100 MHz, as shown in Fig. 5(c). With the increasing bias, the phenomenon of modal competition becomes more obvious due to the more severe SHB by the enhanced stimulated recombination [26], [28]. MPN will seriously limit the performance of the OFDM transmission in the low-frequency region. Fig. 5(d) demonstrates the trend of the resonance frequency increasing with the bias current. The D factor is 5.55 GHz/mA$^{0.5}$ obtained from linear fitting.

B. Original 4-QAM and 16-QAM OFDM Carried by MM-VCSEL Under Bias Current Optimization

The transmission performances of the 30-GHz 4-QAM OFDM data carried by the MM-VCSEL under different bias currents are depicted in Fig. 6. The bias current will significantly affect the transmission performance because the modulation throughput, 3 dB bandwidth, transverse mode, RIN/MPN of the MM-VCSEL are relative to the bias current. The SNR spectra of the MM-VCSEL operated at different bias currents are shown in Fig. 6(a). Because the MM-VCSEL operated at 8 mA does not exhibit the completely flattened and widened frequency throughput, the SNR spectrum shows a drop at the high-frequency region. By increasing the bias current to 12 mA, the SNR spectrum can be enhanced because of the extended modulation bandwidth induced by the bias current. However, the overall SNR spectrum decreases due to the thermal roller

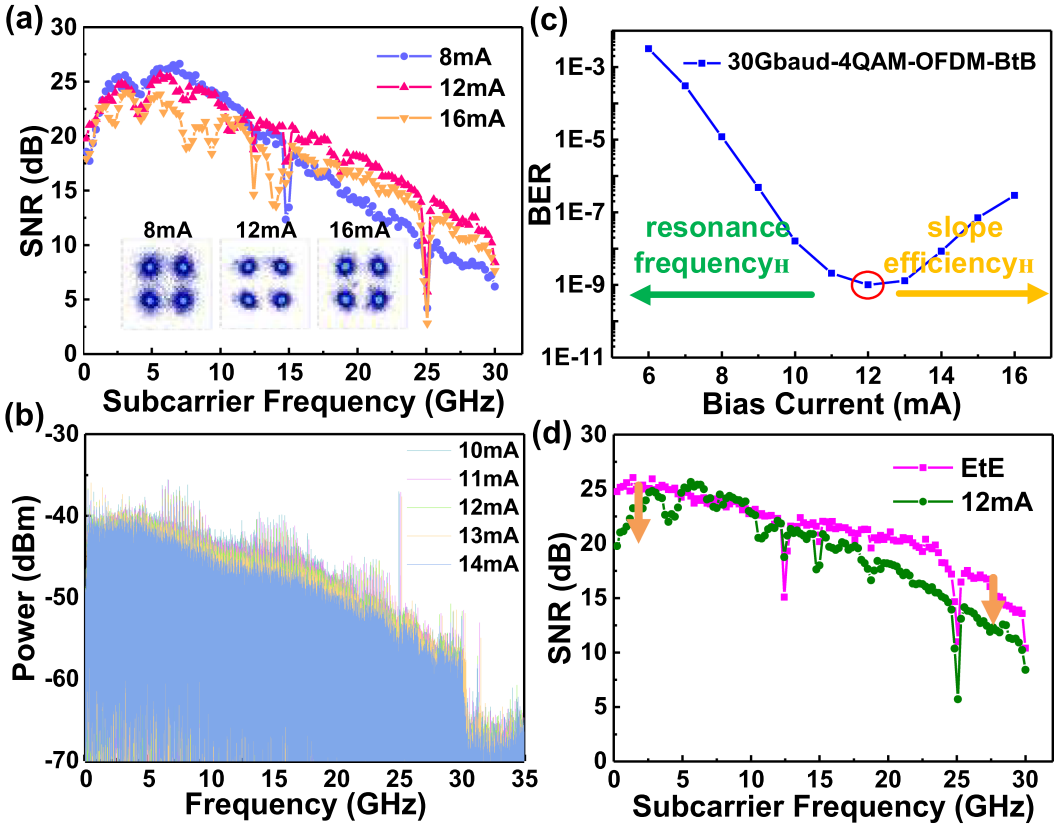

Fig. 6. The (a) SNR spectra, (b) power spectra, and the (c) BERs of 30-GHz 4-QAM-OFDM data carried by the MM-VCSEL operated at different bias currents. (d) The SNR spectra of the electrical and optical 30-GHz 4-QAM-OFDM data.

over effect occurring at 16 mA. The constellation plots of the 30-GHz 4-QAM OFDM data carried by the MM-VCSEL operated at 8 and 16 mA are more blurred than those at 12 mA. Fig. 6(b) illustrates the RF spectra of the 30-GHz 4-QAM OFDM data carried by the MM-VCSEL operated under different bias currents. By increasing the bias current, the overall RF spectrum of the 30-GHz 4-QAM OFDM data slightly decreases because of the power saturation under the high bias current. The BERs of the 30-GHz 4-QAM OFDM data carried by the MM-VCSEL operated under different bias currents are shown in Fig. 6(c).

Because the modulation bandwidth of the MM-VCSEL expands with increasing the bias current to improve the transmission performance in the high-frequency region, the BER of the 30-GHz 4-QAM OFDM data reduces from 10^{-3} to 10^{-9} with increasing the bias current from 6 mA to 12 mA. Then, the BER degrades to 10^{-7} when the bias current of the MM-VCSEL further enlarges to 16 mA because the power saturation induces the low slope efficiency to obtain the worse signal. From the above results, the optimized bias current of the MM-VCSEL is acquired at 12 mA.

Fig. 6(d) demonstrates the SNR spectra of the electrical and optical 30-GHz 4-QAM OFDM data. The AWG and the passive microwave components cause a gradually decreased trend of the SNR spectrum for the electrical 30-GHz 4-QAM OFDM data. When the VCSEL is operated at 12 mA, the noise peak in the RIN spectrum is buried in shot noise to affect the transmission. However, the SNR in the high-frequency region for the optical 30-GHz 4-QAM OFDM data is lower than that for the electrical 30-GHz 4-QAM OFDM data because of the insufficient response of the MM-VCSEL-OM5 MMF transmission system. In the low-frequency region, the SNR of the optical 30-GHz 4-QAM OFDM data is degraded. This SNR degradation is induced by MPN from 10 MHz to 100 MHz, as confirmed in Fig. 5(c).

The transmission performances of the 16-QAM OFDM data transmission delivered by the MM-VCSEL over BtB and 100-m OM5-MMF are shown in Fig. 7. The received RF spectra of the 28-GHz 16-QAM OFDM data transmitted by the MM-VCSEL under optimized bias current in BtB and 100-m OM5 MMF cases are illustrated in Fig. 7(a). Without pre-distortion technology, serious propagation loss during the OM5 MMF transmission contributes to the degraded SNR spectrum. The SNR spectra and corresponding constellation plots of the 28-GHz 16-QAM OFDM data transmitted by the MM-VCSEL in BtB and 100-m OM5 MMF cases are displayed in Fig. 7(b).Because the attenuated signal amplitude and the modal dispersion contribute to the signal distortion, the constellation plot spreads and overlaps with the adjacent mapping coordinate and leads to worse signal quality. This spreading constellation plot effectively degrades the overall SNR spectra. Fig. 7(c) demonstrates the BERs of the 16-QAM OFDM data under different data bandwidths in the BtB and 100-m OM5 MMF cases. As the data bandwidth increases, the insufficient modulation bandwidth and modal dispersion in the MM-VCSEL-OM5 MMF transmission system limit the

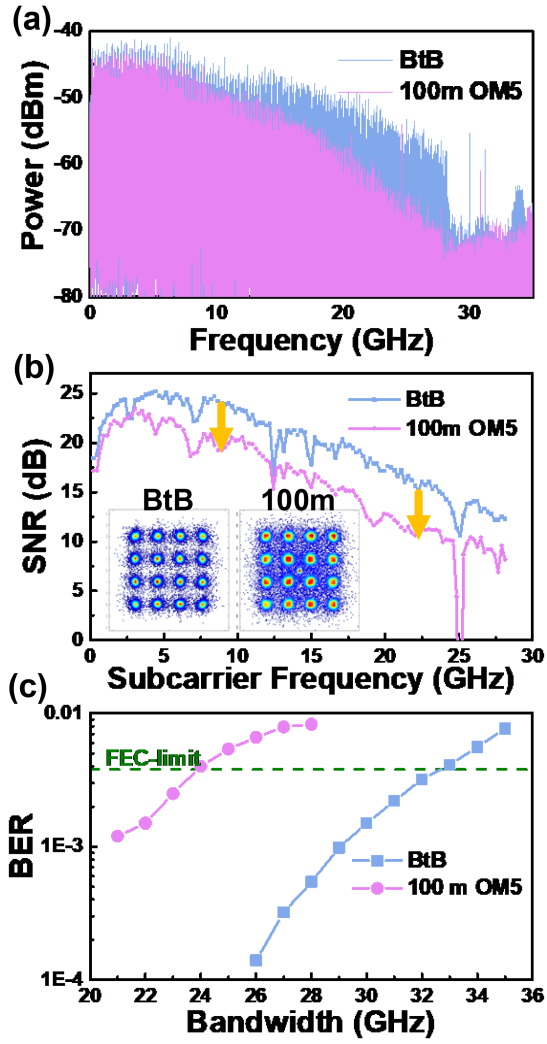

Fig. 7. The (a) power spectra, the (b) SNR spectra, and the constellation plots in 28GHz 16-QAM-OFDM carried by MM-VCSEL in BtB/100-m OM5-MMF cases. (c) The BERs of the 16-QAM OFDM data under different data bandwidths in the BtB and 100-m OM5 MMF cases.

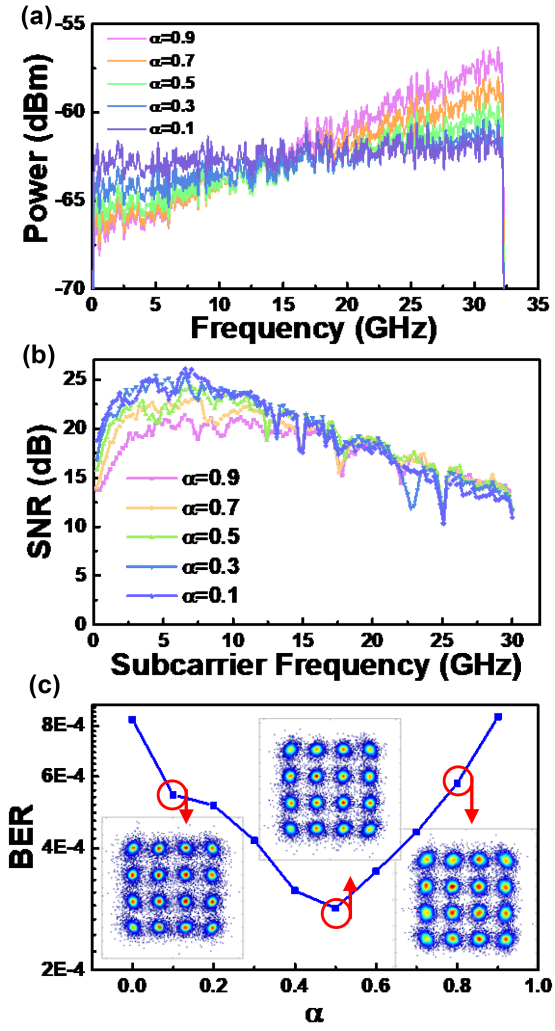

Fig. 8. The (a) RF spectra at the transmitted end, (b) SNR spectra at the received end, and the (c) average BER of the 30-GHz 16-QAM-OFDM data under different pre-leveling factors in the BtB case.

whole transmission capacity to obtain the worse BER. In the BtB case, the MM-VCSEL can deliver the 32 GHz 16-QAM OFDM data with a corresponding data rate of 128 Gbit/s and a BER of 3.2×10^{-3} to meet the FEC criterion of 3.8×10^{-3}. After 100-m OM5 MMF transmission to induce the propagation loss and the modal dispersion, the MM-VCSEL can only transmit the 23-GHz 16-QAM OFDM data with a corresponding data rate of 92 Gbit/s data rate and a BER of 2.4×10^{-3}.

C. Pre-leveled 16-QAM OFDM Carried by the MM-VCSEL

A pre-distortion technique called pre-leveling is used to compensate for the insufficient response of VCSEL [29]. The pre-leveling technology is multiplying the signal spectrum by a rising exponential function. The signal power in the high-frequency region can be pre-compensated before the digital signal is sent to an AWG to generate the electrical analog signal. Therefore, the power attenuation in the high-frequency region during transmission can be resolved by using the pre-leveling technology. The power spectra of the electrical 16-QAM OFDM data under the different pre-leveling factors are depicted in Fig. 8(a). When the pre-leveling factor (a) is set as 0.9, the pre-leveling slope can be estimated as 0.3 dB/GHz. By adjusting the pre-leveling slope, the best pre-compensated condition can be found. The SNR spectra of the 30 GHz 16-QAM OFDM under different pre-leveling factors are illustrated in Fig. 8(b). The overcompensation at a pre-leveling factor of 0.9 sacrifices too much power in the low-frequency region to compensate for the energy in the high-frequency region. This phenomenon degrades the SNR in the middle- and low-frequency regions. With a pre-leveling factor of 0.1, the signal distortion induced by the modulation bandwidth also degrades the SNR spectrum. The BERs of the 30 GHz 16-QAM OFDM under different pre-leveling factors are exhibited in Fig. 8(c). By setting a pre-leveling factor of 0.5, the MM-VCSEL delivers the 30 GHz 16-QAM OFDM data with the most distinguished constellation plot to obtain the lowest BER of 2.84×10^{-4}.

The RF spectra of the 30 GHz 16-QAM OFDM data carried by MM-VCSEL with and without the pre-leveling process in

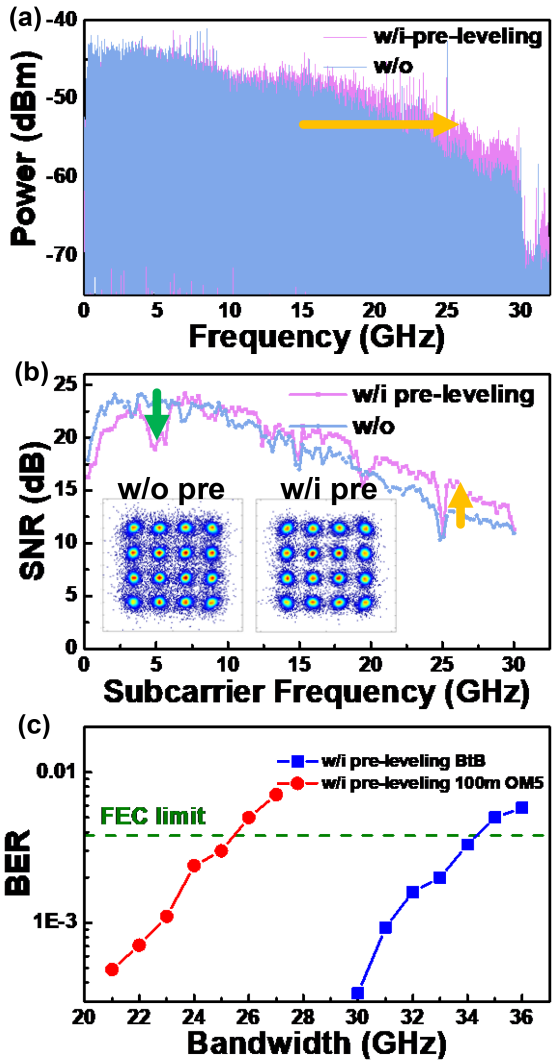

Fig. 9. The (a) RF spectra, (b) SNR spectra, and constellation plots of the 30-GHz 16-QAM-OFDM data carried by the MM-VCSEL with and without pre-leveling technology in the BtB case. (c) The BERs of the 16-QAM-OFDM data carried by the MM-VCSEL with pre-leveling technology under different data bandwidths in the BtB and 100-m OM5 OMF cases.

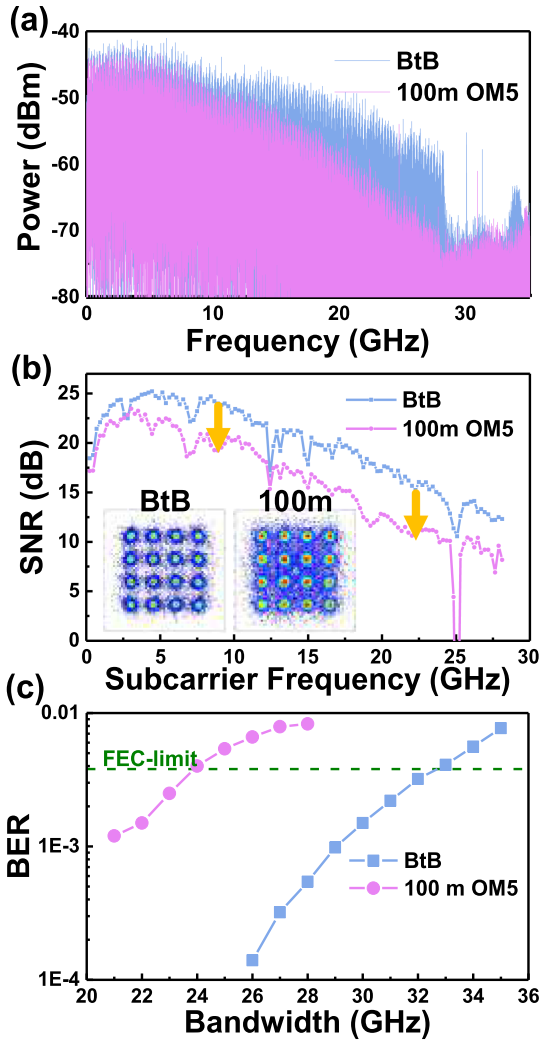

Fig. 10. The (a) RF spectra, (b) SNR spectra, and constellation plots of the 30-GHz 16-QAM-OFDM data carried by the MM-VCSEL with and without pre-emphasis technology in the BtB case. (c) The BERs of the 16-QAM-OFDM data carried by the MM-VCSEL with pre-emphasis technology under different data bandwidths in the BtB and 100-m OM5 OMF cases.

the BtB case are shown in Fig. 9(a). Because the signal power is compensated in the high-frequency region at the transmitting end, the 30 GHz 16-QAM OFDM data has a relatively flat RF spectrum with the pre-leveling process as shown in Fig. 9(a). To compare the transmission performances of the 30 GHz 16-QAM OFDM data with the pre-leveling process, their SNR spectra are shown in Fig. 9(b). At frequencies below 7 GHz, the sacrificed power in the low-frequency region with the pre-leveling technology for a flatter SNR spectrum leads to a lower SNR than that without the pre-leveling process. The BERs of the 16-QAM-OFDM data carried by the MM-VCSEL with pre-leveling technology under different data bandwidths in the BtB and 100-m OM5 OMF cases are demonstrated in Fig. 9(c). The maximal data bandwidth of the 16-QAM OFDM data with the pre-leveling compensation in the BtB case is achieved at 34 GHz (136 Gbit/s) with a BER of 3×10^{-3}. After 100-m MMF transmission to induce the propagation and modal dispersion, the maximal allowable bandwidth decreases to 25 GHz (100 Gbit/s) with a corresponding BER of 3.3×10^{-3}. After adopting the pre-leveling technique, the data bandwidths of the 16-QAM OFDM data are increased by 2 GHz in both BtB and 100-m MMF cases.

D. Pre-emphasized 16-QAM OFDM Carried by the MM-VCSEL

Pre-emphasis technology is another pre-distortion technique to compensate for the uneven power spectrum by multiplying the inverse function of the channel response at the transmitting end [30]. The RF spectra of the 30-GHz 16-QAM OFDM data carried by the MM-VCSEL with and without the pre-emphasis process in the BtB case are depicted in Fig. 10(a). After the pre-emphasis compensation, the 30-GHz 16-QAM OFDM data obtains an entirely flat RF spectrum. However, the amplitude of the time-domain waveform is attenuated to degrade the SNR in

the low-frequency region by using the pre-emphasis process, as shown in Fig. 10(b).

In addition to the sacrificed amplitude, the MPN also makes the SNR in the low-frequency region worse than that in the high-frequency region. The constellation plot of the 30-GHz 16-QAM OFDM data transmitted by the MM-VCSEL gets concentrated but has a larger settlement after the pre-emphasis compensation. Moreover, the BERs of the QAM-OFDM data carried by the MM-VCSEL in the BtB and 100-m OM5 MMF under different data bandwidths after pre-emphasis compensation are illustrated in Fig. 10(c). After the pre-emphasis compensation, the MM-VCSEL can deliver the 34-GHz (136-Gbit/s) 16-QAM OFDM data with a corresponding BER of 3.1×10^{-3} in the BtB case. After the 100-m OM5 MMF transmission, the maximal bandwidth of the 16-QAM OFDM data is achieved at 25 GHz with a data rate of 100 Gbit/s and a BER of 3.6×10^{-3}. The more precise compensation is accomplished by the inverse function of the entire channel response to overcome the severe power fading effect. However, the amplitude of the time-domain waveform is significantly reduced to induce the overall SNR degradation. Therefore, the allowable data capacity under the pre-emphasis compensation is equivalent to that under the pre-leveling process.

The transmission performances of the QAM-OFDM data carried by the MM-VCSEL under the pre-leveling and pre-emphasis processes are compared in Fig. 11. The SNR spectra of the optical 34 GHz 16-QAM-OFDM with and without the pre-leveling and pre-emphasis compensation are described in Fig. 11(a). In the BtB case, the BER of the 34-GHz QAM OFDM data carried by the MM-VCSEL without the compensation technique cannot achieve the FEC criterion. By using the pre-emphasis technology, the SNR spectrum of the optical data has the flattest response because the inverse function of channel response is performed to compensate for the whole frequency response. This phenomenon also contributes to the significant difference in the RF spectrum in the low- and high-frequency regions. However, the only slight difference between the RF spectra in the low- and high-frequency regions for the data transmission with and without the pre-emphasis compensation can be observed. The corresponding constellation plots are also presented in Fig. 11(a) to discuss the high-speed transmission performance. The constellation plot of the 16-QAM OFDM data under the pre-emphasis compensation is more continuous and has a clearer boundary than that under the pre-leveling compensation because of a relatively flattened response during transmission. However, the sacrificed signal amplitude induces a lower SNR to spread the converged points in the constellation plot. The BERs of the 16-QAM OFDM data under different data bandwidths with and without the pre-leveling and pre-emphasis compensation in the BtB and 100-m OM5 MMF cases are shown in Fig. 11(b). In the BtB case, the data bandwidth of the 16-QAM OFDM data can be enhanced from 32 GHz (128 Gbit/s) to 34 GHz (136 Gbit/s) by using the pre-leveling or pre-emphasis compensation. For the 100-m OM5 MMF transmission, the pre-leveling or pre-emphasis compensation also extends the data bandwidth from 23 GHz (92 Gbit/s) to 25 GHz (100 Gbit/s). Although the penalties of 36 Gbit/s for the allowable data rate between BtB and 100-m OM5 MMF cases are the same in all cases, the pre-leveling and pre-emphasis compensation can increase the whole data bandwidth as well as the data rate.

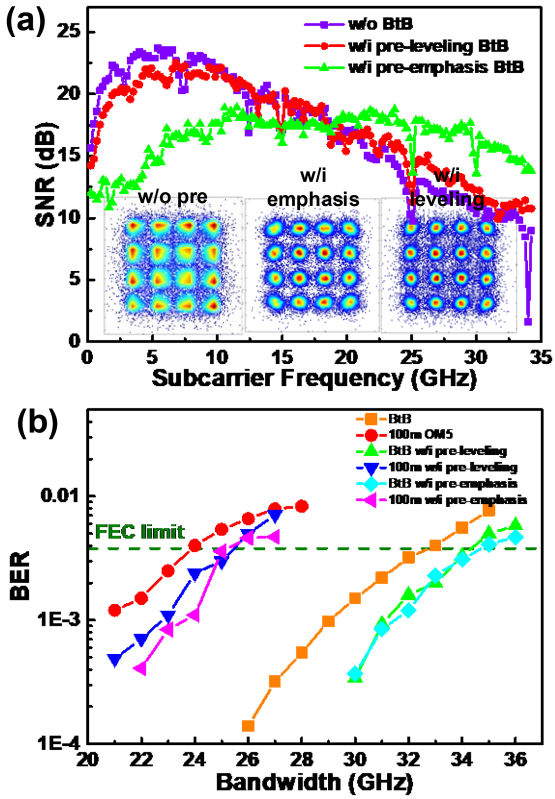

Fig. 11. (a) The SNR spectra and the constellation plots of the 34-GHz 16-QAM-OFDM with and without the pre-leveling and pre-emphasis compensation in the BtB case. (b) The BERs of the 16-QAM OFDM data under different data bandwidths with and without the pre-leveling and pre-emphasis compensation in the BtB and 100-m OM5 MMF cases.

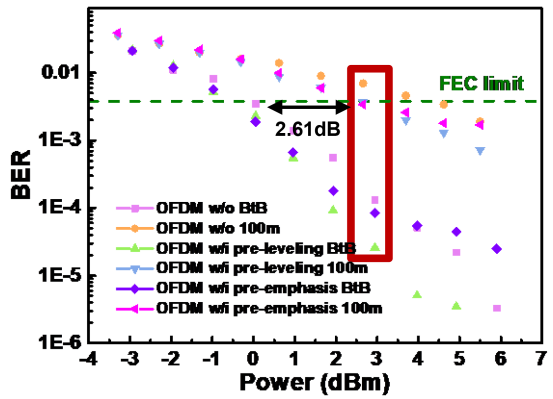

Fig. 12. BERs of the 23-GHz 16-QAM-OFDM with and without the pre-leveling and pre-emphasis compensation under different receiving powers.

The power penalties of the optical 23 GHz 16-QAM-OFDM with and without the pre-leveling and emphasis compensation are demonstrated in Fig. 12. Without the signal compensation, the MM-VCSEL can deliver the 23 GHz 16-QAM OFDM data with the receiving power sensitivities of 0.05 dBm in BtB case and 4.62 dBm in 100-m OM5 MMF case. The power penalty can

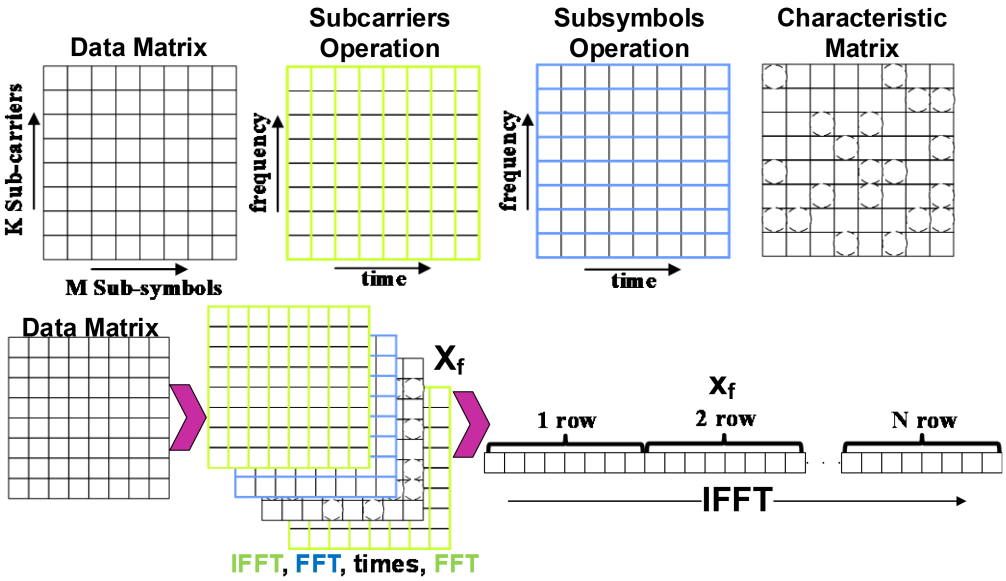

Fig. 13. Time/frequency transformation matrix implementation in GFDM.

be obtained as 4.57 dB for the 23-GHz 16-QAM OFDM data without the signal compensation. For the pre-leveling compensation, the receiving power sensitivity of the 23 GHz 16-QAM OFDM data can be acquired as 2.66 dBm in the 100-m OM5 MMF case, which achieves a power penalty of 2.61 dB. For the pre-emphasis compensation, the results of the receiving power sensitivities are similar to those under the pre-leveling compensation. In the piratical transmission, the optical signal power below 0.05 dBm is not enough to effectively carry the signal even though the optical signal can be converted by the PD with a high conversion efficiency. At the receiving power of 3 dBm, the BER of 1.3×10^{-4} with the signal compensation, the BER of 2.6×10^{-5} with the pre-leveling compensation, and the BER of 8.5×10^{-5} with pre-emphasis compensation can be observed for 23-GHz 16-QAM OFDM transmission in the BtB case. The same data stream with a receiving power of 0.62 dBm over the 100-m OM5 MMF, the BERs are degraded to 1.4×10^{-3} without pre-compensation, 5.5×10^{-4} after pre-leveling, and 6.7×10^{-4} after pre-emphasis. Both the pre-leveling and pre-emphasis compensation can effectively improve the BERs but the pre-leveling compensation still has a better capacity to obtain the low BER in high-speed transmission.

E. 16-QAM GFDM Carried by the MM-VCSEL With [K, M] Parametric Optimization for PAPR and OOB Reduction

An illustration of a GFDM matrix with K = 128 and M = 4 (with presetting N = K×M = 512 as constant in this work) is depicted in Fig. 14(a). Fig. 14(b) shows the RF spectra of the 30-GHz GFDM data with different K conditions. The respective OOBRs of the 30-GHz GFDM data under different K conditions can be observed. As compared to OFDM data, a lower side-lobe level can be obtained by more complicated operations. The more significant main-lobe ripple is correlated to Gibb's phenomenon in GFDM data format [31]. The OOBR suppression ratio under the highest main-lobe level of −50 dBm can be observed at 12.1 dB in K = 256 and 19 dB in K = 16.

TABLE I
THE PAPR AT CCDF = 0.1 AND SIDELOBE LEVEL IN DIFFERENT K SETTINGS

GFDM	K = 512 M = 1	K = 256 M = 2	K = 32 M = 16	K = 16 M = 32	K = 4 M = 128
PAPR (dB) (CCDF@0.1)	11.5	11.4	11.1	10.6	9.4
OOBR level (dBm)	–61.7	–62.1	–66.3	–68.2	–70.4

The complementary cumulative distribution functions (CCDFs) of the PAPRs for the OFDM data and the GFDM with different K conditions are shown in Fig. 14(c). The PARR in dB for the OFDM and GFDM data can be defined as [32]:

$$\mathrm{PAPR(dB)} = 10\log_{10}\frac{\max_{0\le t\le T_s}\left[|x(t)|^2\right]}{E\left[|x(t)|^2\right]}, \qquad (18)$$

where $x(t)$, $E\{\cdot\}$, and T_s respectively denote the time-domain waveform, the expectation value, and the time duration of the symbol. The PAPR of the OFDM data is obtained as 11.44 dB under the CCDF of 0.1. With increasing the K number to 4, the PAPR significantly degrades to 9.37 dB. Low PAPR avoids nonlinear distortion and improves the efficiency of the power amplifier. As a result, Table I summarizes the PAPR and OOBR of the received and decoded data.

With a one-tap equalizer in the frequency domain, there are lower PAPRs and lower side-lobe levels in low K conditions. However, there is also a trade-off between transmission capacity and low OOBR/PAPR because of the insufficient equalizer. Therefore, the setting of the K number needs to be optimized in actual transmission to obtain the low PAPR and high transmission capacity. When K = 512, GFDM is equivalent to OFDM, which has the characteristics of large PAPR and

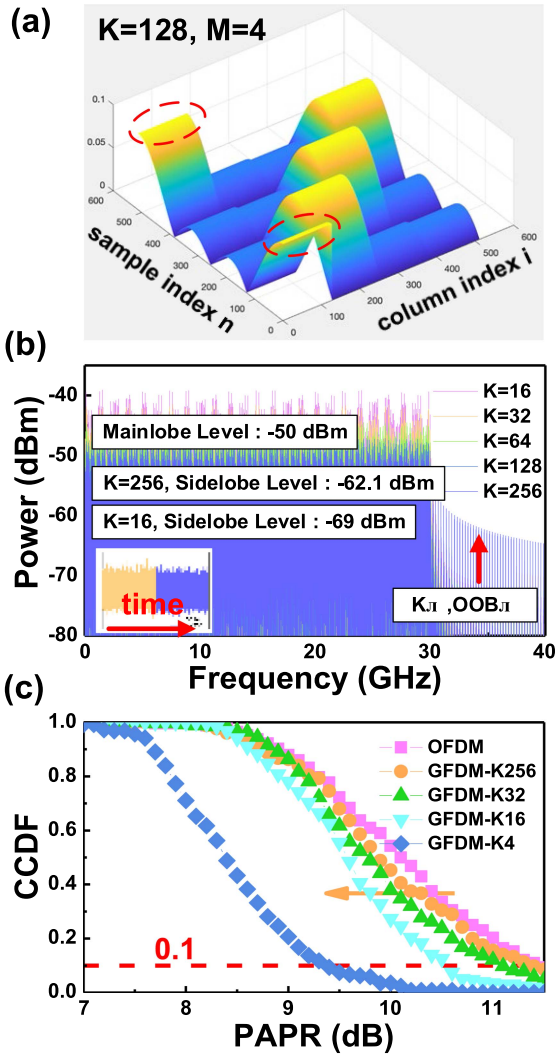

Fig. 14. (a) The pulse shaping in GFDM matrix with K = 128 and M = 4. The (b) RF spectra and the (c) CCDFs of PAPR for the GFDM data with different K conditions.

large OOBR. When K = 1, GFDM is equivalent to SC. A flexible modulation strategy can be achieved by adjusting the K value of GFDM. When K = 512/256/32/16/4, the PAPR is 11.5/11.4/11.1/10.6/9.4 dB at the CCDF = 0.1, and the sidelobe levels are -61.7/-62.1/-66.3/-68.2/-70.4 dBm respectively.

The SNR spectrum of 30 GHz 4-QAM-GFDM with K = 256 and M = 2 is displayed in Fig. 15(a). Because the FFT size is set as 512 points and a sampling rate of the AWG is designed at 120 GS/s, the 30-GHz 4-QAM-GFDM data corresponds to 128 resource elements which are equivalent to distributing these resource elements into 2 sub-symbols and 64 subcarriers in one sub-symbol. Because the shaping filter in the first sub-symbol limits the primary energy by the demodulated block edge, the SNR spectrum in the first sub-symbol is less than that in the second sub-symbol. The notches in the SNR spectrum are suffered from the fixed-frequency noise in the real-time scope, as shown in Fig. 15(a). This phenomenon cannot be avoided by one-tap equalization to slightly affect transmission performance. The SNR spectrum of the 30 GHz 4-QAM-GFDM with K = 128 and M = 4 is shown in Fig. 15(b). The 128 resource elements are divided into 4 sub-symbols and 32 resource elements are distributed for each sub-symbol. The SNR spectrum of the 30 GHz 4-QAM-GFDM data with K = 64 and M = 8 is illustrated in Fig. 15(c). To improve the efficiency of the power amplifier, the QAM-GFDM modulation with a larger M number exhibits a low PAPR. On the other hand, more resource elements are distributed into the first sub-symbol to cause the rapidly degraded BER by decreasing the M number. Besides, more resource elements are degraded by the fixed-frequency noise with increasing the M numbers. The BERs of the 30-GHz 4-QAM-GFDM data with different K numbers are depicted in Fig. 15(d). Therefore, the K number of 128 and M value of 4 for the 30-GHz 4-QAM-GFDM data is optimized to obtain the lowest BER of 3.1×10^{-4}. Further increasing the M inevitably causes the BER degradation over the FEC criterion.

The SNR spectrum and the constellation plot of the 22-GHz 16-QAM GFDM data carried by the MM-VCSEL with (K, M) of (128, 4) in the BtB case are depicted in Fig. 16(a). The SNR of the 22-GHz 16-QAM GFDM data transmitted by the MM-VCSEL is followed by the frequency response of the whole VCSEL-based transmission system. The unavoidable defect in demodulation deteriorates the transmission result in the first sub-symbol. The enhanced noise by the non-orthogonal resource element also degrades the overall SNR. Because the resource element distribution skips the specific subcarrier corresponding to the spurious noise frequency in real-time scope, the representation of the data rate for the QAM-GFDM data in this work is utilized to replace the modulation bandwidth. The relationship between BER and data rate for the 16-QAM GFDM data in BtB and 100-m OM5-MMF cases is demonstrated in Fig. 16(b). The 22-GHz 16-QAM GFDM data delivered by the MM-VCSEL with a data rate of 88 Gbit/s can be achieved with a corresponding BER of 2.4×10^{-3} in the BtB case. The maximal modulated bandwidth of the 16-QAM GFDM data reduces to 17 GHz (68 Gbit/s) with a corresponding BER of 3.6×10^{-3} after 100-m OM5 MMF transmission. The BERs of the QAM-OFDM and QAM-GFDM data under different data bandwidths in the BtB and 100-m OM5 MMF cases are demonstrated in Fig. 16(c). From the transmission results, the GFDM data format is less suitable for ultra-high-speed transmission than the OFDM data format because of the insufficient one-tap equalizer compensation induced by the non-orthogonal characteristic in GFDM modulation and the first sub-symbol defect in demodulation. However, a minimum mean square error (MMSE) equalizer can be used to improve the shortage of one-tap equalization in GFDM demodulation, which further obtains the low PAPR characteristic.

The BERs of the 14-GHz 16-QAM GFDM data transmitted by the MM-VCSEL in the BtB and 100-m OM5 MMF cases are exhibited in Fig. 17. The MM-VCSEL can deliver the 14 GHz 16-QAM GFDM data with a receiving power sensitivity of 0.05 dBm and a BER of 3.6×10^{-3} in the BtB case. After 100-m OM5 MMF transmission, the receiving power sensitivity and BER of the 14-GHz 16-QAM GFDM data are degraded to 5.5 dBm and 1.2×10^{-3}, contributing to a power penalty of 5.45 dB. The signal broadening induced by dispersion leads to

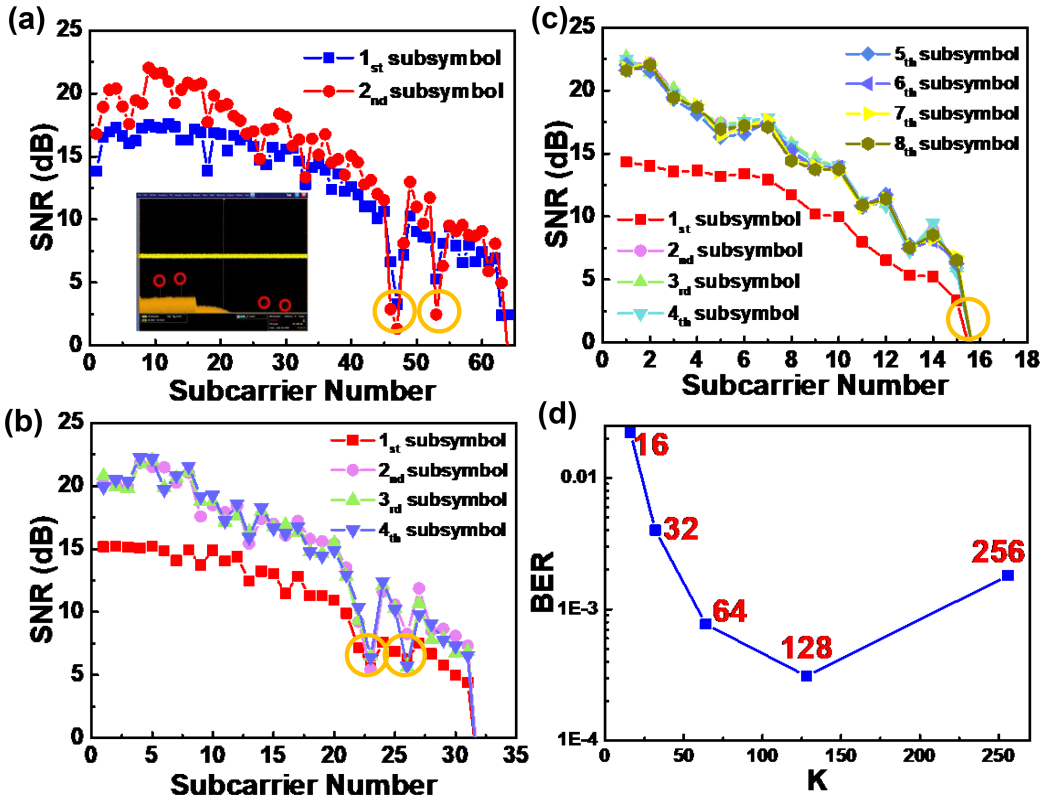

Fig. 15. The SNR spectra of 30 GHz 4-QAM-GFDM data with (a) (K, M) = (256, 2), (b) (K, M) = (128, 4), and (c) (K, M) = (64, 8). (d) The BERs of 30 GHz 4-QAM-GFDM data by different K numbers.

distortion in the time domain to limit the transmission capacity in GFDM without the MMSE equalizer. Because of the insufficient equalizer of the GFDM data format, the power penalty of GFDM is larger than that of OFDM.

F. Bit-Loading DMT Data Carried by the MM-VCSEL With Adaptive Bit Allocation Strategy

The greedy algorithm is a strategy to take the current most favorable choice in every selection and divide the problem into several sub-problems. Then, the local optimization of each sub-problem is combined into a solution of the original problem, as shown in Fig. 18(a). The greedy algorithm can be used to solve some issues with less precision quickly. According to the Shannon-Hartley theorem, the maximal transmission volume as the target data rate in the greedy-based self-adaptive algorithm is predicted by the estimated SNR performance in the current channel. The maximal transmission capacity in the current channel by Shannon-Hartley theorem can be represented as [33], [34]:

$$DataRate_{\max} = \sum_{i=1}^{N} B \cdot \log_2\left(1 + \frac{S_i}{N_i}\right), \qquad (19)$$

where N is the number of subcarriers in OFDM, B is the subcarrier bandwidth, S_i is the average received signal power in each subcarrier, and N_i is the average power of the noise and interference in each subcarrier. According to the latest channel estimation results, the data is distributed into the sub-channel with the most SNR margin to determine via the discrepancy between the resulting SNR and the required SNR in the current modulated QAM level. Then, the target data rate can be achieved, as shown in Fig. 18(b).

For the maximal spectral usage efficiency, the adaptive QAM mapping is used to distribute different bit levels according to the transmission characteristics for each subcarrier. First, the SNR spectrum in the channel by 16-QAM OFDM transmission is adopted as shown in the blue line in the upper part of Fig. 19. Then, the bit distributed in subcarriers by the self-adaptive algorithm can slightly change the allocation strategy by adjusting the limitation between different QAM levels. Because the response of VCSEL limits the performance of unstable subchannels in high frequency, the QAM level lower than 4-QAM is not considered for transmission. The SNR notches suffering from the fixed noise in the real-time scope can be distributed lower QAM level or skipped by the algorithm to improve the overall BER. The total data rate can be evaluated by the formula of $\{Sa \times [\ \Sigma N_{MQAM} \times \log_2(M)] / S_{FFT}\}$. Adaptive QAM mapping facilitates the MM-VCSEL to deliver the bit-loaded DMT data at 145 Gbit/s in the BtB case. Among them, 32/16/8/4 QAM mappings are considered at this time. The subcarrier suffered from the spurious noise in the SNR notch at 25 GHz is distributed in the 4-QAM level and failed with the FEC criterion. The SNRs and BERs can be respectively obtained as 19.1 dB and 1.6×10^{-3} for 32-ary QAM DMT data, 15.3 dB and 3.3×10^{-3} for 16-ary QAM DMT data, 12.3 dB and 2.8×10^{-3} for 8-ary QAM DMT data, 6.8 dB and 1.4×10^{-2} for 4-ary QAM DMT data. Except that the 4-QAM data allocated at the highest subcarrier frequency band

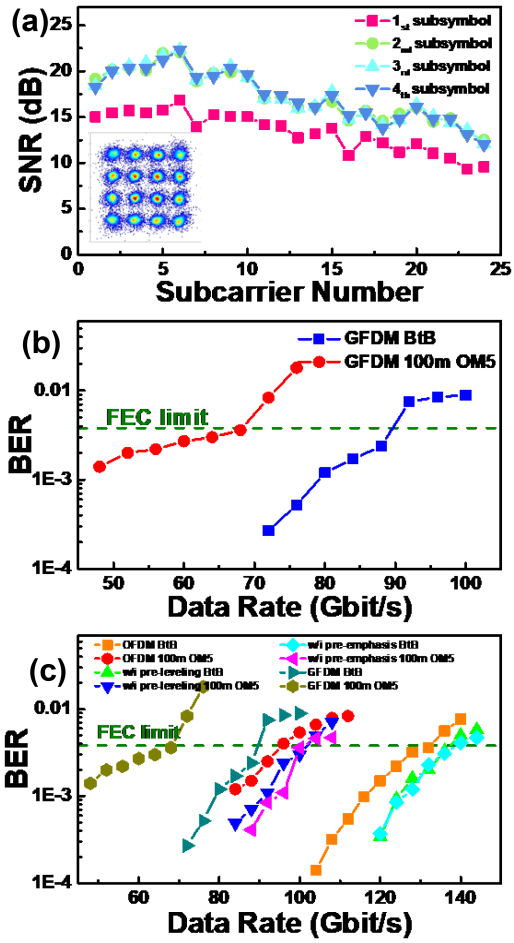

Fig. 16. (a) The SNR spectrum of 22-GBaud 16-QAM-GFDM data carried by the MM-VCSEL in the BtB case. (b) The BERs of the 16-QAM-GFDM data transmitted by the MM-VCSEL under different data rates in the BtB and 100-m OM5-MMF cases. (c) The comparison of the transmission performance between the QAM-OFDM and GFDM data with different data rates in BtB and 100-m OM5 MMF cases.

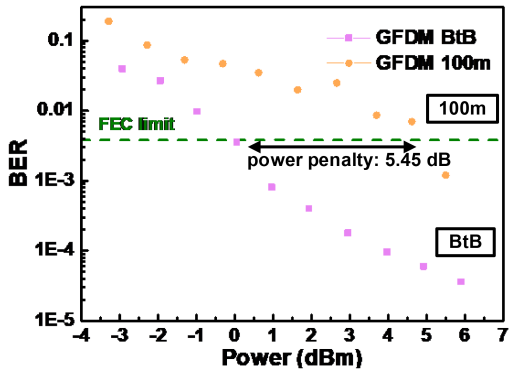

Fig. 17. The average BER versus receiving power of 14GHz 16-QAM-GFDM.

provides an extremely blurred constellation plot and fails to enter the FEC-requested BER criterion, all other decoded M-ary QAM data reveal relatively clear constellation plots with their qualified receiving BERs listed in the inset of corresponding constellation plots, as shown in the lower part of Fig. 19.

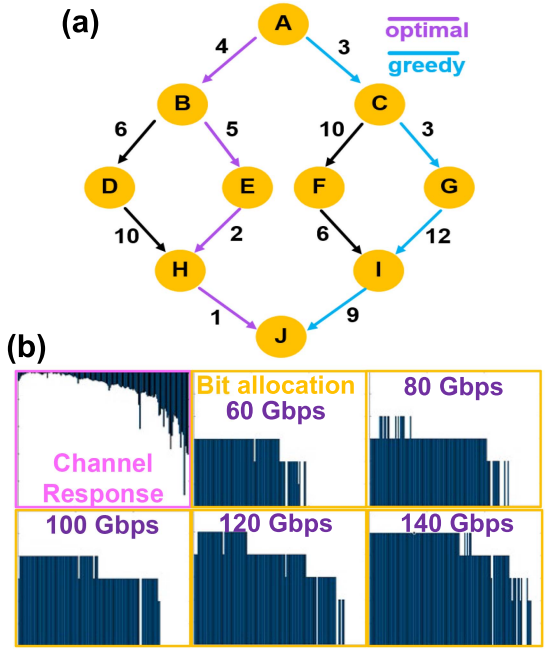

Fig. 18. The (a) graphical greedy algorithm, (b) the process of bit distribution.

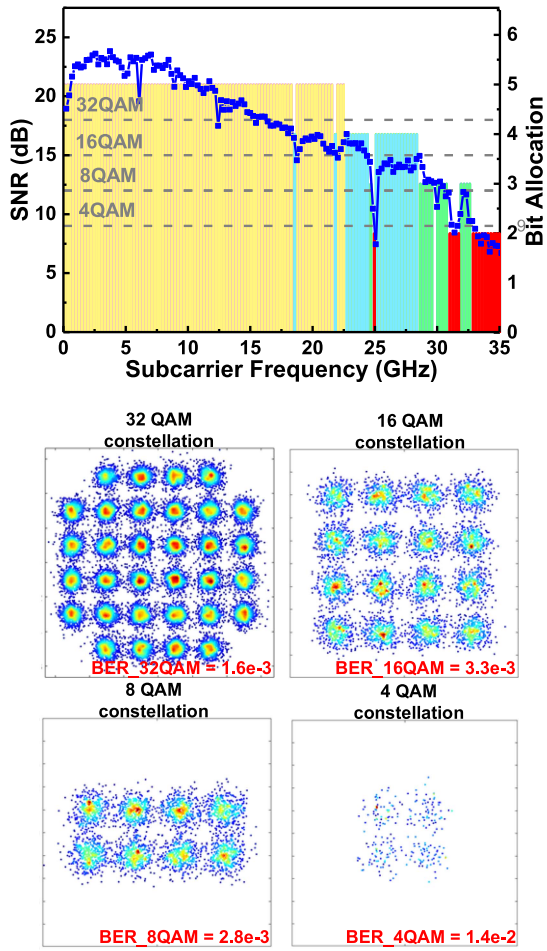

Fig. 19. The bits allocation, SNR response, and constellation plots for the DMT data with the self-adaptive algorithm at 145 Gbit/s in the BtB case.

TABLE II
THE MAXIMAL BAUD RATE AND DATA RATE OF DIFFERENT FORMATS CARRIED BY THE MM-VCSEL

Format	OFDM	GFDM	OFDM	OFDM	DMT
Algorithm	original	[K, M] [128, 4]	pre-level	pre-emphasis	bit-loading
QAM Level (M-ary)	16	4	16	16	32/16/8/4
Bandwidth (GBaud)	32	30	34	34	35
Data Rate (Gbit/s)	128	120	136	136	145

At last, the maximal allowable baud rate and data rate of different OFDM/GFDM/DMT formats carried by the MM-VCSEL are listed in Table II for a fair comparison without adding channel response. Without employing additional algorithms for data processing, the MM-VCSEL can only provide 32-GBaud bandwidth for carrying the original 16-QAM OFDM data up to 128 Gbit/s. The MM-VCSEL fails to offer a large bandwidth for the GFDM owing to the unexpected notch response between the grouped GFDM spectral components in the frequency domain. By applying either the pre-leveling or the pre-emphasizing algorithm, the declined modulation response of the MM-VCSEL can be compensated to allow 34-GBaud data transmission at 136 Gbit/s. When comparing with all of the single M-ary broadband OFDM/GFDM formats without or with pre-distortion, the bit-loading DMT format can manipulate the whole allowable bandwidth with multi-level QAM data to fit with the SNR at different carrier frequencies. As a result, such an adaptive bit-loading algorithm greatly improves the deliverable data rate up to 145 Gbit/s.

In contrast to previous reports, the experimental results of this work implemented using MM-VCSEL are promising not only because of the comparison among new formats/algorithms but also because of the achievement of their relatively high Baud rates. In general, both current-injecting and photon-emitting areas of the MM-VCSEL are quite large to limit its allowable encoding bandwidth, which subtly sets a trade-off between the lasing mode number and the encodable bandwidth for traditional data format. Fortunately, the advanced data format benefits from advantages including spectral utilizing and planning efficiency to greatly improve the data rate of the MM-VCSEL. When considering the bridging of the conversion-free wired and wireless networks at the complicated optical-to-electrical-to-optical circuit interface with simplicity and convenience, the MM-VCSEL with such advanced broadband data coding is undoubtedly the competing candidate in terms of power-efficient cost-effective, and operation, as compared to other state-of-the-art VCSELs with fewer modes but also a lower power.

IV. CONCLUSION

The high-spectral-efficiency modulation techniques for the OFDM/GFDM/DMT data transmitted by the directly modulated 850-nm MM-VCSEL with optimized transmission microstrip design are demonstrated in this work. The optimized VCSEL structure provides a threshold current of 0.65 mA, a maximal optical output power of 3.74 mW, a slope efficiency of 0.28 in the linear region, a differential resistance of 63 Ω, a reflection coefficient of 0.11, a return loss of 19.1 dB, and a voltage standing wave ratio of 1.24 dB, and a D factor of 5.55 GHz/mA$^{0.5}$. The MM-VCSEL operated at $20I_{\mathrm{th}}$ still exhibits about 6-7 transverse modes, its RIN raises to −146.9 dBc/Hz at 12 mA with increased damping response, and its MPN also degrades the SNR by 0–2 dB. Under the optimized bias current, the BERs of the QAM-OFDM data delivered by the MM-VCEL can be achieved at 128 Gbit/s in the BtB case and 92 Gbit/s after 100-m OM5-MMF transmission. After the pre-leveling compensation with a pre-leveling slope of 0.5 dB/GHz, the data rates can be improved to 136 Gbit/s in the BtB case and 100 Gbit/s after 100-m OM5-MMF transmission. With the pre-emphasis technique, the improvement in data rate is similar to that under the pre-leveling compensation with an increment of 8 Gbit/s in the BtB and 100-m OM5-MMF cases. For low PAPR characteristics in transmission, the GFDM data format with (K, M) of (128, 4) is optimized by the trade-off between BER and low PAPR to demonstrate the 88-/68-Gbit/s data transmission in the BtB/100-m OM5 MMF cases. Nevertheless, the DMT data format is adopted to maximize the efficiency of spectral utilization by adaptive QAM mapping in bit distribution with a self-adaptive algorithm. Only 32/16/8 QAM levels are considered in the experiment because the subchannels with low SNR are unstable to carry the data. The total data rate successfully reaches 145 Gbit/s under BtB with the corresponding BERs of 1.6×10^{-3}/3.3×10^{-3}/2.8×10^{-3} in 32/16/8 QAM, respectively. As compared to the 16-QAM OFDM transmission without any pre-distortion technique, the improvement of the data rate can be achieved to 17 Gbit/s by using the bit-loaded DMT data. The various modulation schemes, including the pre-distortion compensation, GFDM modulation with low PAPR and OOBR, and the DMT with maximum spectral efficiency, are demonstrated to provide a more flexible modulation strategy for integrating the seamless network in the future.

REFERENCES

[1] Cisco Annual Internet Report (2018-2023), Mar. 2020. [Online]. Available: http://www.cisco.com/c/en/us/solutions/collateral/executive-perspectives/annual-internet-report/white-paper-c11-741490.html
[2] K.-Y. Cheng, *III-V Compound Semiconductors and Devices*, 1st ed. Berlin, Germany: Springer, 2020.
[3] A. Mutig, "High speed VCSELs for optical interconnects," Ph.D. dissertation, Institut für Festkörperphysik, Technische Universität Berlin, Berlin, Germany, 2010.
[4] H.-Y. Kao et al., "Comparison of single-few-multi-mode 850 nm VCSELs for optical OFDM transmission," *Opt. Exp.*, vol. vol. 25, no. 14, pp. 16347–16363, 2017.
[5] S. Kandula, S. Sengupta, A. Greenberg, P. Patel, and R. Chaiken, "The nature of data center traffic: Measurements and analysis," in *Proc. ACM Internet Meas. Conf.*, 2009, pp. 202–208.
[6] J. Mata et al., "Artificial intelligence (AI) methods in optical networks: A comprehensive survey," *Opt. Switching Netw.*, vol. 28, pp. 43–57, Apr. 2018.
[7] M. Zhang, C. You, H. Jiang, and Z. Zhu, "Dynamic and adaptive bandwidth defragmentation in spectrum-sliced elastic optical networks with time-varying traffic," *J. Lightw. Technol.*, vol. 32, no. 5, pp. 1014–1023, Mar. 2014.
[8] S. K. Singh and A. Jukan, "Machine-learning-based prediction for resource (Re)allocation in optical data center networks," *J. Opt. Commun. Netw.*, vol. 10, no. 10, pp. D12–D28, Oct. 2018.

[9] G. Fettweis, M. Krondorf, and S. Bittner, "GFDM-generalized frequency division multiplexing," in *–2009 IEEE 69th Veh. Technol. Conf.*, 2009, pp. 1–4.
[10] N. Michailow, I. Gaspar, S. Krone, M. Lentmaier, and G. Fettweis, "Generalized frequency division multiplexing: Analysis of an alternative multi-carrier technique for next generation cellular systems," in *Proc. Int. Symp. Wireless Commun. Syst.*, 2012, pp. 171–175.
[11] C. Browning et al., "5G wireless and wired convergence in a passive optical network using UF-OFDM and GFDM," in *Proc. IEEE Int. Conf. Commun. Workshops*, Paris, France, 2017, pp. 386–392.
[12] I. Gaspar et al., "GFDM-A framework for virtual PHY services in 5G networks," 2015. [Online]. Available: https://arxiv.org/abs/1507.04608
[13] C.-L. Tai, B. Su, and P.-C. Chen, "Optimal filter design for GFDM that minimizes PAPR under performance constraints," in *Proc. IEEE Wireless Commun. Netw. Conf.*, Barcelona, Spain, Apr. 2018, pp. 1–6.
[14] P.-C. Chen and B. Su, "Filter optimization of out-of-band radiation with performance constraints for GFDM systems," in *Proc. 18th IEEE Int. Workshop Signal Process. Adv. Wireless Commun.*, Jul. 2018, pp. 1–5.
[15] P.-C. Chen, B. Su, and Y. Huang, "Matrix characterization for GFDM: Low complexity MMSE receivers and optical filters," *IEEE Trans. Signal Process.*, vol. 65, no. 18, pp. 4940–4955, Sep. 2017.
[16] H.-Y. Wang, C.-H. Cheng, C.-T. Tsai, Y.-C. Chi, and G.-R. Lin, "28-GHz wireless carrier heterodyned from orthogonally polarized tri-color laser diode for fading-free long-reach MMWoF," *J. Lightw. Technol.*, vol. 37, no. 13, pp. 3388–3400, Jul. 2019.
[17] P. T. Dat, A. Kanno, N. Tamamoto, and T. Kawanishi, "Seamless convergence of fiber and wireless system for 5G and beyond networks," *J. Lightw. Technol.*, vol. 37, no. 2, pp. 592–605, Jan. 2019.
[18] P. T. Dat, A. Kanno, N. Tamamoto, and T. Kawanishi, "Full-duplex transmission of LTE-A carrier aggregation signal over a bidirectional seamless fiber-millimeter-wave system," *J. Lightw. Technol.*, vol. 34, no. 2, pp. 691–700, Jan. 2016.
[19] T. N. Duong et al., "Adaptive loading algorithm implemented in AMOOFDM for NG-PON system integrating cost-effective and low-bandwidth optical devices," *IEEE Photon. Technol. Lett.*, vol. 21, no. 12, pp. 790–792, Jun. 2009.
[20] P. S. Chow, J. M. Cioffi, and J. A. C. Bingham, "A practical discrete multitone transceiver loading algorithm for data transmission over spectrally shaped channels," *IEEE Trans. Commun.*, vol. 43, no. 2/3/4, pp. 773–775, Feb./Mar./Apr. 1995.
[21] Y. Zhang and K. Letaief, "Multiuser adaptive subcarrier-and-bit allocation with adaptive cell selection for OFDM systems," *IEEE Trans. Wireless Commun.*, vol. 3, no. 5, pp. 1566–1575, Sep. 2004.
[22] J. Campello, "Optimal discrete bit loading for multicarrier modulation systems," in *1998 IEEE Int. Symp. Inf. Theory*, Cambridge, MA, USA, Aug. 1998, p. 193.
[23] A. Mutig and D. Bimberg, "Progress on high-speed 980 nm VCSELs for short-reach optical interconnects," *Adv. Opt. Technol.*, vol. 2011, 2011, Art. no. 290508.
[24] J. Y. Law and G. P. Agrawal, "Mode-partition noise in vertical-cavity surface-emitting lasers," *IEEE Photon. Technol. Lett.*, vol. 9, no. 14, pp. 437–439, Apr. 1997.
[25] R. Schatz and M. Peeters, "Modeling spatial-hole burning and mode competition in index-guided VCSELs," *Proc. SPIE*, vol. 4942, pp. 158–169, 2002.
[26] J. Wilk, R. P. Sarzala, and W. Nakwaski, "The spatial hole burning effect in gain-guided VCSELs," *J. Phys. D: Appl. Phys.*, vol. 31, 1998, Art. no. L11.
[27] A. Valle and L. Pesquera, "Mode partition noise in multi-transverse mode vertical-cavity surface-emitting lasers," *Proc. SPIE*, vol. 3625, pp. 414–425, 1999.
[28] C.-L. Lo, "The spatiotemporal modeling of oxide-confined vertical-cavity surface-emitting lasers," M.S. thesis, Dept. Photonics., National Yang-Ming Chiao Tung Univ., Hsinchu, Taiwan, 2004.
[29] H.-Y. Kao et al., "Few-mode VCSEL chip for 100-Gbs transmission over 100 m multimode fiber," *Photon. Res.*, vol. 5, pp. 507–515, Oct. 2017.
[30] K. Szczerba, T. Lengyel, M. Karlsson, P. A. Andrekson, and A. Larsson, "94-Gb/s 4-PAM using an 850-m, VCSEL, pre-emphasis, and receiver equalization," *IEEE Photon. Technol. Lett.*, vol. 28, no. 22, pp. 2519–2521, Nov. 2016.
[31] L. R. Rabiner, "Techniques for designing finite-duration impulse-response digital filters," *IEEE Trans. Commun. Technol.*, vol. CT-19, no. 2, pp. 188–195, Feb. 1971.
[32] D. Wulich, "Definition of efficient PAPR in OFDM," *IEEE Commun. Lett.*, vol. 9, no. 9, pp. 832–834, Sep. 2005.
[33] C. E. Shannon and W. Weaver, *The Mathematical Theory of Communication*. Champaign, IL, USA: Univ. Illinois Press, 1949.
[34] C. E. Shannon, "Communication in the presence of noise," *Proc. IRE*, vol. 37, no. 1, pp. 10–21, Jan. 1949.